ORIGINAL ARTICLE

Evaluation of computational fluid dynamics models for predicting pediatric upper airway airflow characteristics

Yicheng Chen[1] · Xin Feng[2,3] · Xieqi Shi[2,4] · Weihua Cai[1,5] · Biao Li[1] · Yijun Zhao[1]

Abstract

Computational fluid dynamics (CFD) has the potential for use as a clinical tool to predict the aerodynamics and respiratory function in the upper airway (UA) of children; however, careful selection of validated computational models is necessary. This study constructed a 3D model of the pediatric UA based on cone beam computed tomography (CBCT) imaging. The pediatric UA was 3D printed for pressure and velocity experiments, which were used as reference standards to validate the CFD simulation models. Static wall pressure and velocity distribution inside of the UA under inhale airflow rates from 0 to 266.67 mL/s were studied by CFD simulations based on the large eddy simulation (LES) model and four Reynolds-averaged Navier–Stokes (RANS) models. Our results showed that the LES performed best for pressure prediction; however, it was much more time-consuming than the four RANS models. Among the RANS models, the Low Reynolds number (LRN) SST k-ω model had the best overall performance at a series of airflow rates. Central flow velocity determined by particle image velocimetry was 3.617 m/s, while velocities predicted by the LES, LRN SST k-ω, and k-ω models were 3.681, 3.532, and 3.439 m/s, respectively. All models predicted jet flow in the oropharynx. These results suggest that the above CFD models have acceptable accuracy for predicting pediatric UA aerodynamics and that the LRN SST k-ω model has the most potential for clinical application in pediatric respiratory studies.

Keywords Upper airway · Cone-beam computed tomography · Computational fluid dynamics · Medical image-based modeling

1 Introduction

Airway diseases, such as adenoid and tonsil swelling, are common and can reduce airway ventilation in children [1], which may lead to obstructive sleep apnea (OSA) and other diseases with severe consequences [2]. Airway diseases and their resulting decreased respiratory capacity are traditionally assessed by imaging examination, endoscopy, polysomnography (PSG), and nasal resistance examination [3–6]. Patients are primarily diagnosed by imaging examination or endoscopy to determine airway morphology and then be recommended to perform ventilation tests by PSG or nasal resistance meter; however, these conventional methods are challenging for clinicians because of high costs, complex diagnostic processes, or poor understanding of the cause of disease. Therefore, more prospective clinical studies and aerodynamic studies are warranted to investigate associations between upper airway (UA) morphology, respiratory function, and clinical symptoms to better understand patients with airway diseases.

In recent years, computational fluid dynamics (CFD) methods have been widely used to investigate the aerodynamic features of human airways [7–9] using patient volumetric imaging data; for example, data acquired by cone-beam computed tomography (CBCT) [10]. Rapid predictions of respiratory

✉ Weihua Cai
caiwh@neepu.edu.cn

✉ Biao Li
biaoli@hit.edu.cn

1 School of Energy Science and Engineering, Harbin Institute of Technology, Harbin, China

2 Department of Clinical Dentistry, Section for Oral and Maxillofacial Radiology, University of Bergen, Bergen, Norway

3 Faculty of Medicine, University of Oslo, Oslo, Norway

4 Department of Oral Maxillofacial Radiology, Faculty of Odontology, Malmö University, Malmö, Sweden

5 School of Energy and Power Engineering, Northeast Electric Power University, Jilin City, China

aerodynamic features by CFD and understanding their associations with airway morphology and ventilation could provide considerable assistance to surgeons for patient management [5, 11–13]. Therefore, using CFD based on patient-specific image scan data may be an ideal procedure for surgeons to quickly assess an individual's aerodynamics and the causes of respiratory problems without invasive endoscopy [14].

Nevertheless, the clinical application of CFD in respiratory diagnosis in various populations has been limited due to a lack of experimental validation of simulation methods. The simulation methods of CFD can significantly influence prediction results, which makes it essential to study the appropriate turbulence model to precisely predict the airflow inside of human UA before clinical application [15]. Three simulation methods are commonly applied in turbulence modeling of CFD: direct numerical simulation (DNS), large eddy simulation (LES), and Reynold-averaged Navier–Stokes (RANS). DNS and LES are generally considered to have good accuracy that can resolve large-scale airflow motion when the computational grids used are sufficiently fine, especially the DNS can resolve all scales [16–20]. The long computational time is currently one of the cons of DNS and LES methods, which a more powerful computing system may overcome in the future. Many previous clinical studies have applied RANS models, as these models require less time and computational resources than LES and DNS [13, 21–26]; nevertheless, the RANS models will time-average airflow turbulence and reduce the temporal and spatial resolution of airflow simulations. Therefore, the clinical application of RANS models on human airways should be discussed based on experimental results.

To our knowledge, few experimental studies have validated turbulence models for use in pediatric UA. For adult UA, the estimated Reynolds number varies from 800 to over 12,000 under different breathing conditions [27, 28]. Some studies have indicated that the standard k-ω model has the best overall performance among RANS models for studying airflow in enlarged nasal cavities [18, 29]. Phuong and Xu both performed validation studies in the adult trachea by particle image velocimetry (PIV) but reached different conclusions regarding the optimal RANS model for this purpose [30, 31]. Phuong suggested the Abe-Nagano-Kondoh (LR-ANK) k-ε model, while Xu selected the RNG k-ω and SST k-ω models. In a wall static pressure test experiment in complete adult UA, Mylavarapu reported that the standard k-ω model was the best option among RANS models under an extremely high flow rate [32]. As the pediatric airway is usually smaller in diameter and has a lower inspiratory airflow rate than adults' [33], it has a lower estimated range of Reynolds number from 930 to 2420 [6, 34], which may cause more transitional airflows than adult UAs. Therefore, it is critical to test and verify computational models specifically for this young group of patients before clinical application.

This study aimed to propose a CFD simulation strategy that best represents in vivo airflow characteristics of pediatric UAs. The performances of four RANS methods were evaluated by both in vitro pressure, and PIV measurements in a pediatric UA model imaged using CBCT.

2 Materials and methods

2.1 Image acquisition and UA model construction

The patient in this study was a 13-year-old boy with adenoid and mild tonsil hypertrophy diagnosed by CBCT imaging. His clinical features were not assessed, including respiratory symptoms and nasendoscopy examination. CBCT scan data were retrospectively selected and used as a 3D model of the upper airway (3D eXam; KaVo, Biberach an der Riss, Germany). The recorded scanning parameters were 120 kV and 5 mA, with a scanning time of 14.7 s. Voxel size was 0.2 mm, and each layer was scanned at a 0.2-mm interval, with 14-bit pixel depth and 13×17-cm field of view. During image acquisition, the patient was asked to sit and breathe peacefully without swallowing or mouth breathing. The CBCT scan was exported in digital imaging and communications in medicine format for further analysis.

The airway boundary was defined using a grayscale threshold from − 1024 to − 800 (approximately − 1000 Hounsfield units for air region) using Mimics software (Materialise, Belgium). A 3D segmented UA model was then obtained, which included the nasal cavity, bilateral maxillary sinus, nasopharynx, velopharynx, oropharynx, and laryngopharynx. The UA contour was smoothed three times using the built-in algorithm (Fig. 1). In this study, the inlet (nostril) and outlet (base of the epiglottis) were elongated to 3 mm and 30 mm, respectively, to avoid reverse flow in simulations [35].

2.2 Grid independence and CFD procedures

A computational UA model was obtained by filling the air space in the segmented UA model with tetrahedral grids (ANSYS, Inc., Canonsburg, PA). Five layers of hexahedral grids were used as prism layers to resolve the viscous sub-layer. The flow rate at rest breathing for children has rarely been mentioned in previous reports; for grid independence tests, an inhale flow rate of 200 mL/s was chosen, according to one previous study [36]. The grid independence of the turbulence model under the RANS framework was verified (Fig. 2) by studying the pressure difference between probe 6 (P6) and probe 1 (P1) under different mesh resolutions. Finally, grid 2, which had a body grid size of 0.5 mm and a height of the first element in the prism layer of 10 μm, was selected for RANS simulation. Grid 5, with the same
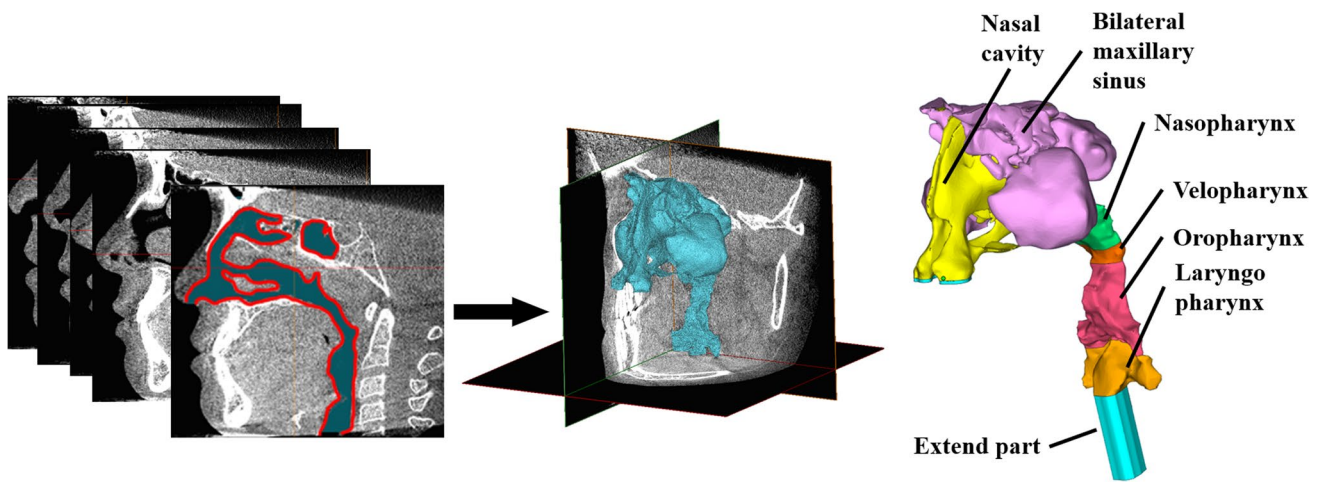
Fig. 1 Process of 3D upper airway reconstruction from CBCT scans

body grid size (0.3 mm) previous LES study [17], was used for LES simulation.

During simulations, the pressure at the nostril inlet was set as zero, and the airflow rate at the outlet was controlled. The UA boundary was considered non-slip, stationary, and rigid [23]. The low Reynolds number turbulence (about 930 to 2420 in the pediatric airway [6, 34]) induced by stenosis airway structure [37, 38] was resolved using RANS models.

Steady simulations under the reliable grid 2 were performed with a series of Q values: 66.67, 100, 133.33, 166.67, 200, 233.33, and 266.67 mL/s. The numerical RANS simulations under the k-ω model framework were applied in this study using ANSYS Fluent with the standard k-ω, Low Reynolds number (LRN) k-ω, SST k-ω, and LRN SST k-ω models in the steady-state, while the LES model in the transient state was applied using the finest grid. The airflow inside the UA was considered to be incompressible Newtonian fluid with a constant density (ρ) because of the very low Mach number (Ma < 0.02).

A second-order finite-volume scheme was applied to discretize governing equations in the computational domain, and second-order implicit discretization was employed for time integration. The coupling of pressure and velocity was implemented using the SIMPLE algorithm [39]. The Smagorinsky-Lilly subgrid-scale model was applied for LES simulation. The data presented were averaged from 0.3 to 1.2 s, achieving convergent solutions in each time step (time step = $1e^{-5}$ s), as shown in Fig. 3. LES simulation took approximately 80 h in a computer with 16 threads, whereas RANS took < 2 h.
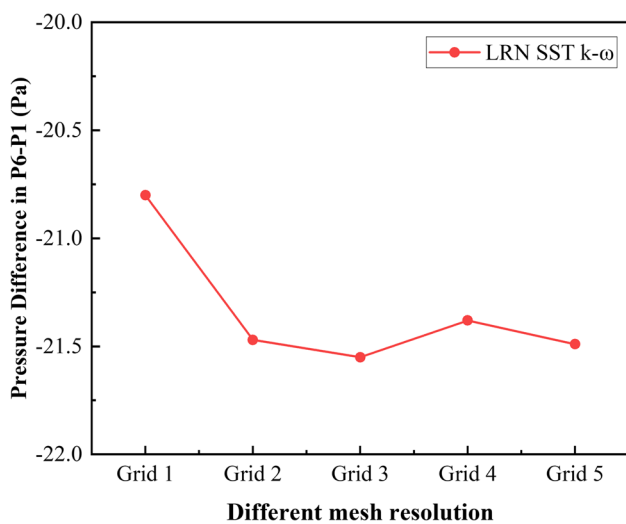

Fig. 2 Grid independence test of RANS simulations in 200 mL/s under different mesh resolutions. Element number and maximum grid size: grid 1, 3.02 million, 0.6 mm; grid 2, 4.52 million, 0.5 mm; grid 3, 13.02 million, 0.4 mm; grid 4, 18.12 million, 0.35 mm; grid 5, 26.80 million, 0.3 mm
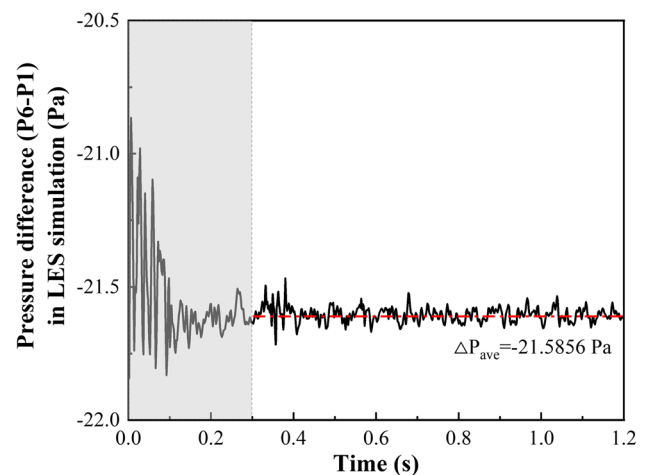

Fig. 3 Instantaneous static pressure difference with a time step of simulation in unsteady LES simulations at an inspiratory airflow rate of 200 mL/s between P6 and P1 (time step = $10.^{-5}$ s)

2.3 Pressure test experiments

To validate CFD simulations, physical experiments were performed using a 3D-printed mechanical UA model with the facility presented in Fig. 4. The mechanical UA model was fabricated by stereo lithography (STL) in actual scale with resin (DSM IMAGE 8000), yielding a uniform thickness of 2 mm, with 0.1-mm roughness. The outlet was connected to a vacuum pump group through two airflow stabilizers. Airflow driven by negative pressure passed through the unrestricted nasal inlet into the mechanical UA model to perform the same aerodynamic process as those in a human UA. An afloat flowmeter was set between stabilizers and the vacuum pump group, simultaneously recording the real-time airflow rate. Nine pressure probes (diameter, 1/32 inch) were mounted on the wall of the experimental model. As shown in Fig. 3, most pressure probes (P2–P9) were located along the posterior and anterior wall downstream of the nasal cavity, while P1 was set near the nostril. Dwyer gage pressure transducers (MS2-W101, Magnesense, USA), with an accuracy of ± 1.0% f.s. and 0–10 VDC output, were installed to measure the wall static pressure difference (ΔP_w) between pressure probes and P1. Error analysis is shown in Appendix 1. The piezoelectric signals from pressure transducers were received by a data collector (Agilent 34972A, Keysight Technologies, USA). The

vacuum pump group was constructed from four diaphragm pumps, which controlled the airflow rate according to a defined power-flow relationship.

2.4 Particle image velocimetry setup

An in vitro airflow field experimental platform was constructed; the apparatus is illustrated in Fig. 5. A transparent UA model, with the same precision described above, was printed using transparent light resin (refractive index (RI), approximately 1.53) and held in a square water chamber. A saturated NaI solution (RI, about 1.49) was injected into the UA model and water chamber to match the refraction. The RI difference between the resin and solution led to laser refraction near the experimental walls (with high curvature); therefore, the observed window was limited to the central part of the airway. A water pump was connected downstream of the airway, and the flow rate was manually controlled while reading the flow meter.

A standard PIV system from Dantec was applied [40]. The experiments used a high-frequency dual-pulse double-exposure CCD camera to quickly capture two flow field images in a relatively short time and record instantaneous flow field characteristics by studying the motions of tracer particles in the images. The PIV technique was employed to measure the velocity distribution in the oropharynx and laryngopharynx, with a dual
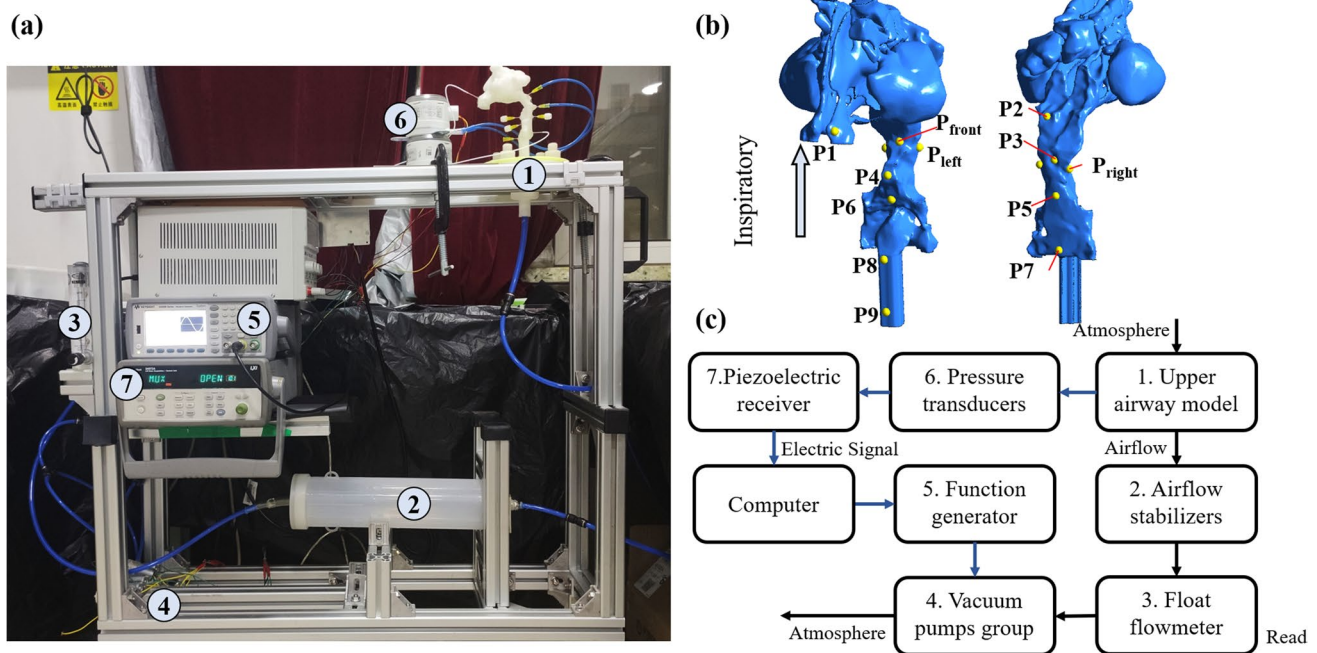

Fig. 4 a Experimental facility for wall static pressure difference measurements in the UA model. (**b**) Mechanical UA models and measurement points. (**c**) Schematic diagram of the experimental facility. ① UA model; ② Airflow stabilizers; ③ Float flowmeter; ④ Vacuum pumps group; ⑤ Function generator; ⑥ Pressure transducers; ⑦ Piezoelectric receiver
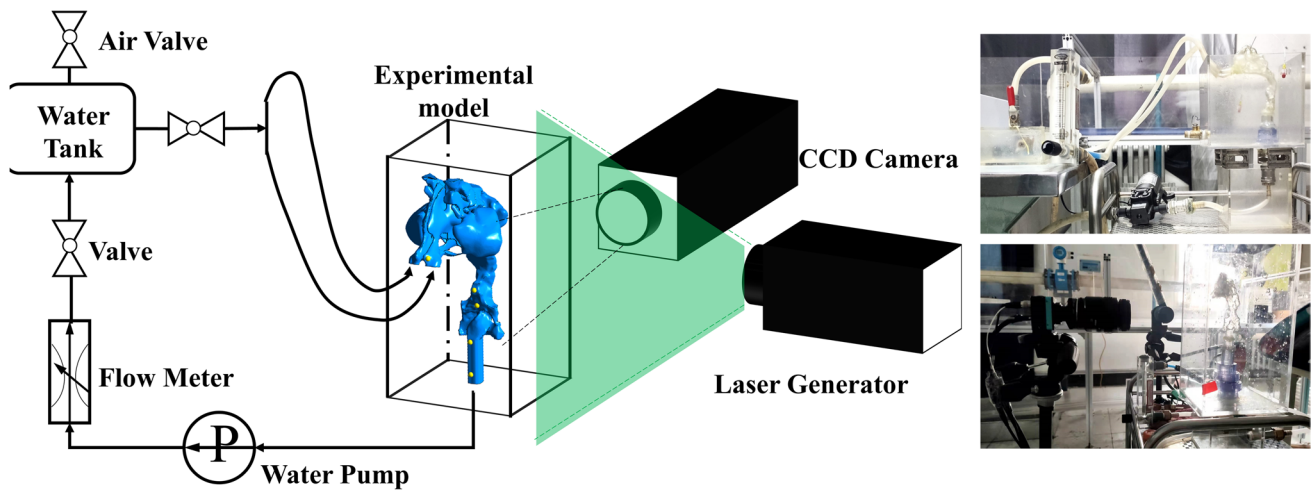
Fig. 5 Schematic of the PIV experimental platform and apparatus setup

200 mJ pulse-1 10 Hz Nd-YAG double-cavity laser illuminating the central sagittal plane of the pharynx. The settings and data postprocessing for PIV equipment are presented in Appendix 2.

To duplicate actual breathing conditions, fluids should have a similar Reynolds number (Re) in both numerical simulations and experimental measurements. The relationship can be described as follows:

$$Q_{\text{solution}} = \frac{\mu_{\text{solution}}\rho_{\text{air}}}{\mu_{\text{air}}\rho_{\text{solution}}}Q_{\text{air}} \qquad (1)$$

where Q_{solution} is volumetric flow rate, ρ is density, and μ is dynamic viscosity. The parameters of NaI solution at 25℃ during experiments were $\rho_{\text{solution}} = 1.904$ g/cm³, $\mu_{\text{solution}} = 3.196 \times 10^{-3}$ Pa s. Q_{solution} was approximately 96 L/h during experiments, which was the same Reynolds number as an airflow rate of 233.33 mL/s in UA. The mean velocity contour shown in (Fig. 9a) was determined using the time-averaged velocity vector field of the pharynx sagittal plane, calculated based on 300 instantaneous velocity vector maps.

3 Results

The wall pressure difference (ΔP_{w}) values at a flow rate of 200 mL/s for the experimental model and its corresponding predictions from the five CFD models at various measuring points are illustrated in Figs. 6 and 7. The ΔP_{w} increased along the airflow direction, with 19.9 Pa (P1–P2) in the posterior wall of the nasopharynx and 37.0 Pa near the outlet (P1–P9). An abnormal decrease of ΔP_{w} was found at P5 and P6, the level of the tongue base and the top of the epiglottis, implying that the air

pressure recovers downstream of the velopharynx, which corresponds to the recirculation flows [41] and split flows caused by the pharyngeal jet [27, 42]. All numerical models used in this study showed similar trends to those of experiments, except for the P4 monitoring point in the anterior wall of the oropharynx. Two models predicted a decrease of ΔP_{w} in P4, while the predictions of the LRN SST k-ω, standard k-ω, and LES models were for an increase, consistent with the experimental results. All CFD models tended to underestimate ΔP_{w}; it was approximately 7% lower using the LES model, 10% lower using LRN SST k-ω and standard k-ω models, and 20% lower using other models for the overall prediction relative to the actual measurement. As shown in Fig. 7, different RANS models showed an apparent discrepancy in
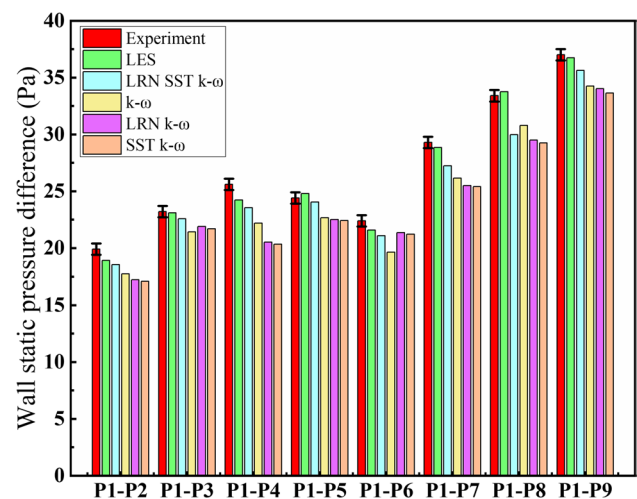

Fig. 6 Comparison of wall static pressure difference with error bar (at the measurement points shown in Fig. 4) between experiments and five CFD models at a fixed inspiratory flow rate of 200 mL/s
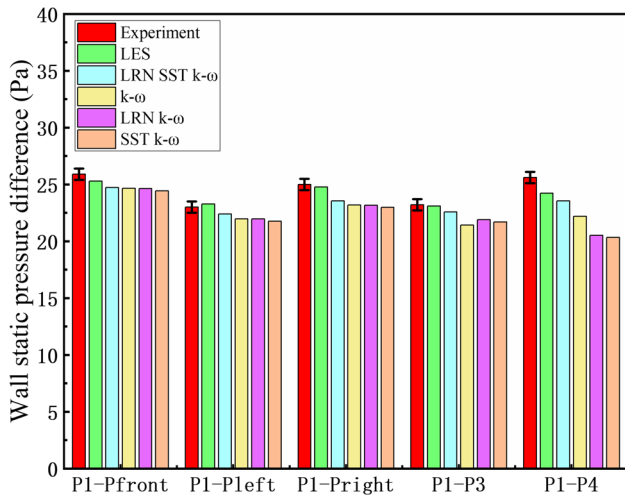
Fig. 7 Comparison of wall static pressure difference with error bar between experiments and five different CFD models at a fixed inspiratory flow rate of 200 mL/s. The measurement points are located around the top of the oropharynx (see Fig. 4)

prediction only close to P4, where there is usually considered to be a region that forms a recirculation bubble. The comparisons of ΔP_w in Figs. 6 and 7 show that the LES and LRN SST $k\text{-}\omega$ models exhibit better agreement with experimental results than the other three RANS models.

CFD predictions and experimental results generated using multiple flow rates varied similarly. ΔP_w at P1–P2 and P1–P8 (Fig. 8a, b) exhibited an increasing trend, growing with nonlinear relationships to both Q and Q^2. CFD simulations still underestimated ΔP_w, and the errors

rose with increasing Q. The LES model performed better than the RANS models, while there was no significant difference in performance as the flow rate increased between the LRN SST $k\text{-}\omega$ and $k\text{-}\omega$ models.

Velocity contours in the sagittal plane are shown in Fig. 9. The laser refraction leads to failure in identifying the near-wall velocity in PIV experiments, but all PIV experiments and CFD simulations generated high velocity in the central part of the airway (Fig. 9), indicating a right-lateral jet flow in the laryngopharynx; however, CFD simulations predicted a longer jet flow. The three cross-sectional velocity profiles presented in Fig. 10 demonstrate that the simulations performed well in predicting maximum velocity while they overestimated jet flow width. The maximum velocity of jet flow in section b′ was 3.617 m/s in PIV, while the corresponding values at the same spatial location were 3.681, 3.532, and 3.439 m/s for the LES, LRN SST $k\text{-}\omega$, and standard $k\text{-}\omega$, respectively.

4 Discussion

There is no consensus on the most representative RANS model for analysis of the pediatric UA, resulting in continuing uncertainty in the clinical diagnosis of respiratory disease using CFD. In this study, CFD simulations were performed in a complete pediatric UA without simplification of airway structures and verified by pressure and velocity distribution measured in vitro physical experiments.
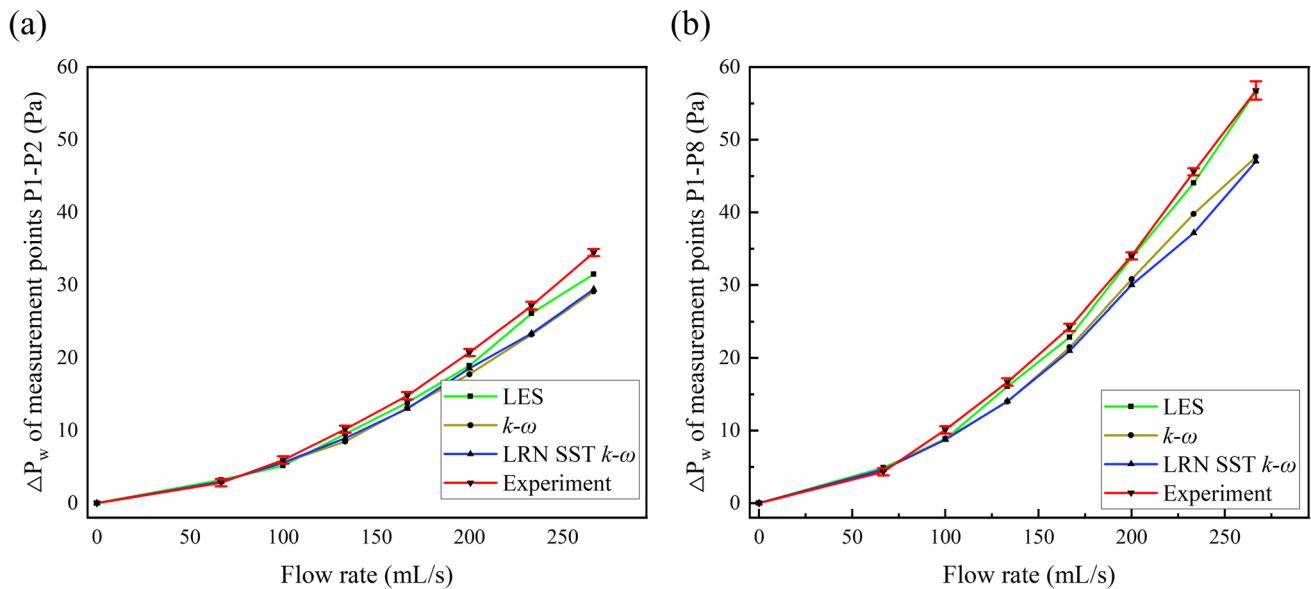

Fig. 8 Comparison of wall static pressure difference between numerical predictions and experimental measurements at various flow rates. (**a**) Wall static pressure difference in nasopharynx at P1-P2. (**b**) Wall static pressure difference in the posterior wall of epiglottis at levels P1-P8

Fig. 9 Velocity contours from PIV and CFD predictions at the sagittal plane of the pharynx (233.3 mL/s). (**a**) Instantaneous and mean velocity contour of PIV, (**b**) Instantaneous and mean velocity contour of LES. (**c**) LRN SST *k-ω*, (**d**) *k-ω*. The maximum velocity of PIV occurs in the center of section b′
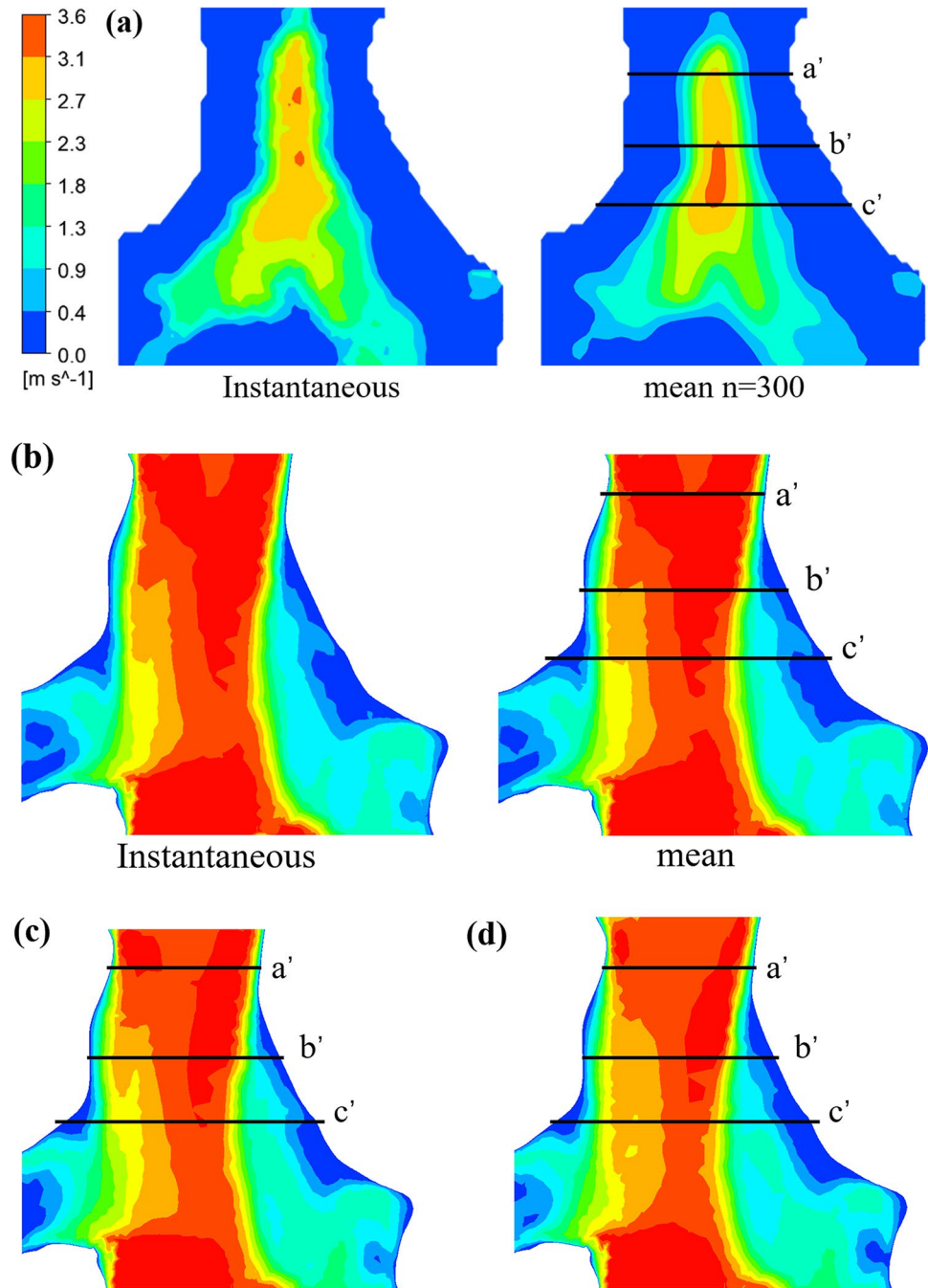
Wall pressure is an important parameter in clinical respiratory diagnosis since it is directly related to airway collapse and ventilation function. This study investigated four CFD models to predict wall pressure and compared the results with experimental results and LES results. The LES model exhibited better performance than RANS models for all flow rates (Figs. 6, 7, and 8), consistent with the previous theory. In this study, the LRN SST *k-ω* model showed the best performance among RANS models, followed by the standard *k-ω* model. This can be partly attributed to better accounting for the transport

of principal turbulence shear stress in adverse pressure gradient boundary-layers under low Reynolds number conditions using the LRN SST *k-ω* model compared with the standard *k-ω* model [43]. Both the LRN SST *k-ω* and standard *k-ω* models showed good consistency with the reference standard, and with the prediction results of the LES model at low flow rates, despite being performed using relatively coarse grids (Fig. 6). Although the prediction errors of these two models increased slightly as the flow rate rose, their trend was consistent with the experimental results (Fig. 8).
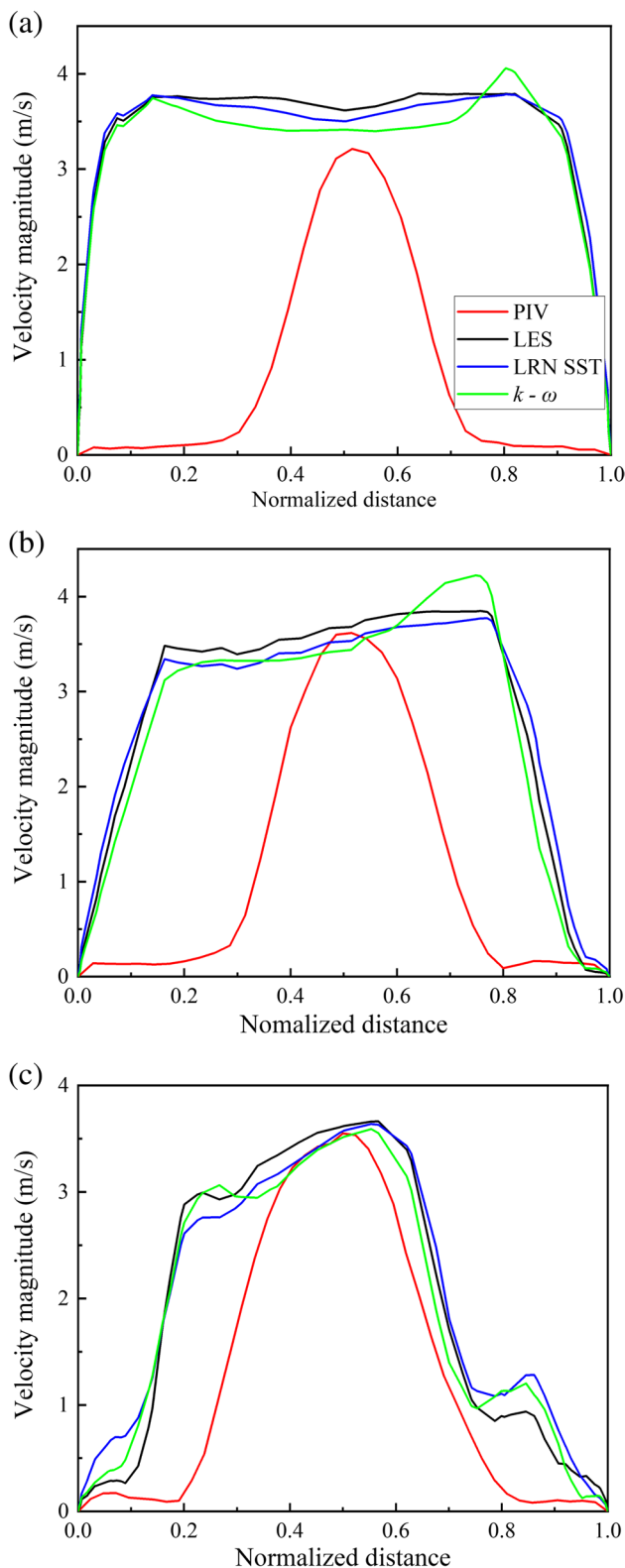
Fig. 10 Cross-sectional velocity profiles of sections a′, b′, and c′. (**a**) CFD simulations present a wider jet flow in the oropharynx. (**b**) Simulations predicted an approximate value in the same location of section b′, which is the maximum velocity of mean PIV. (**c**) PIV and all simulations indicated a right-side jet flow in the laryngopharynx

In previous experimental studies, velocity distribution has been widely applied for flow pattern matching. Some studies have suggested that the SST k-ω model is sufficiently accurate for predicting velocity profiles in the trachea [20, 30, 31]; however, the accuracy of simulations may reduce with a higher Reynolds number or complex UA [18]. Although our experiment failed to capture the near-wall flow field due to laser reflection, both experiments and numerical simulations indicated a pharyngeal jet flow in the central part of the airway (Figs. 9 and 10) [44]. All CFD simulations can roughly predict the maximum velocity in the oropharynx and laryngopharynx, but with a more obvious jet flow than PIV, possibly induced by different viscous diffusion in the pulsing flow between air and NaI solutions [45]. Compared with the standard k-ω model, velocity prediction using the LRN SST k-ω model was closer to that achieved by the LES model. These works support the use of the LRN SST k-ω model to predict pediatric airway aerodynamic characteristics, especially after further validation for near-wall velocity. Hence, the turbulence model and simulation processes applied in this study are an effective CFD simulation strategy that best represents in vivo airflow characteristics of pediatric UA and has the potential for future applications of clinical respiratory research.

This study also yielded some insights useful for the evaluation of UA aerodynamics. In previous investigations [42, 46] and this study, the pressure difference to flow rate ratio was inconsistent as the flow rate varied. These results suggest that the widely used airway resistance equation ($R = \frac{\Delta P}{Q}$) may not be a good indicator for evaluating airway ventilation function at different flow rates [13, 22, 47, 48].

This study has some limitations. The current pilot study employed only one pediatric UA. Future studies with larger cases are warranted to account for the influence of UA anatomical variation among individuals. Furthermore, the inlet and outlet boundary conditions were not patient-specific, and the accuracy of CBCT reconstruction could not be verified due to the study design. Despite these limitations, this is the first study that has tested and verified several CFD models for a pediatric UA. Our data represent a valuable foundation for the development of future clinical applications for CFD in pediatric airway diagnosis.

5 Conclusion

In conclusion, here we introduce two experiments on an image-based actual model of a child's UA as benchmarks and evaluate the overall performance of four RANS models. The LRN SST k-ω model exhibited acceptable accuracy in predicting velocity and ΔP_{w} and performed better than the other three RANS models at fixed flow rates, making it a potential choice for the simulation of pediatric UA in future clinical practice.

Appendix 1

In this study, experimental errors of pressure were tested by time-averaged and repeated measurements. The pressure sensors were set to measure for 1 min and collect the data every 50ms. Each measurement yielded 1200 data points and averaged as a pressure result (see Fig. 11). Two ranges were applied during experiments, the equipment error is ±1% F.S. and drawn by dash lines. More than 98% of data points were within the error range and proved the reliability of the equipment.
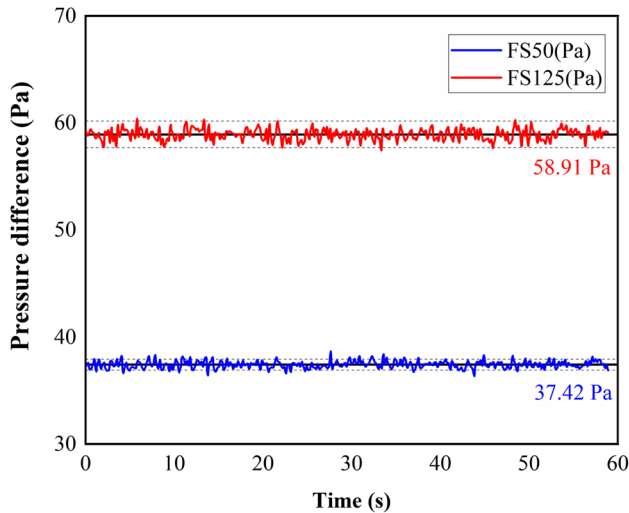

Fig. 11 Time-varied pressure in experiments

To reduce manual error, data were measured five times under the same working condition. The manual errors at different flow rates were as follows (see Table 1), which were much smaller than the equipment error.

Appendix 2

In the PIV measurement of this study, a two-dimensional flow field was measured using polystyrene microspheres (20 µm) as tracers for visualization. A standard PIV system from Dantec was applied. Some parameters of key components in the PIV system were introduced as follows: the double-pulsed Nd-YAG (YAG-yttrium aluminum garnet) lasers with an output of 200 mJ/pulse; the CCD camera (FlowSense 4MEO Model-81C92) with a resolution of 2048×2048 pixels. Here, the area of PIV image was larger than the size of experimental setup to obtain the whole flow field in the convection cell. The interrogation area was set to be 32×32 pixels (with 50% overlap in each direction). The mean density of particles was 1.05 g/cm^3, and their Stokes number was about 0.0088. The thickness of laser light was about 1.0 mm. The time gap between two subsequent image pairs was about 25 ms. Here the diameter of particles was only about 1.25 pixels in the image. The diameter of the particle was close to the estimated pixel size, and the displacements of particles tended to be biased towards integer values in PIV results. The measurements were affected by peak locking. The system error of the image analysis by peak locking was about 0.03 pixels. Therefore, the uncertainty analysis of velocity in PIV measurement was 2%.

The postprocessing of PIV data includes cross-correlation, universal detection, coherence filter, average filter, and moving average validation. The cross-correlation and universal detection adopt recommended settings, but the limited radius to be 30 pixels in the Coherence filter. Set the box size of the average filter and moving average validation was 3×3 and 5×5, separately. Time-varying velocity measurement at fixed points is shown in Fig. 12.
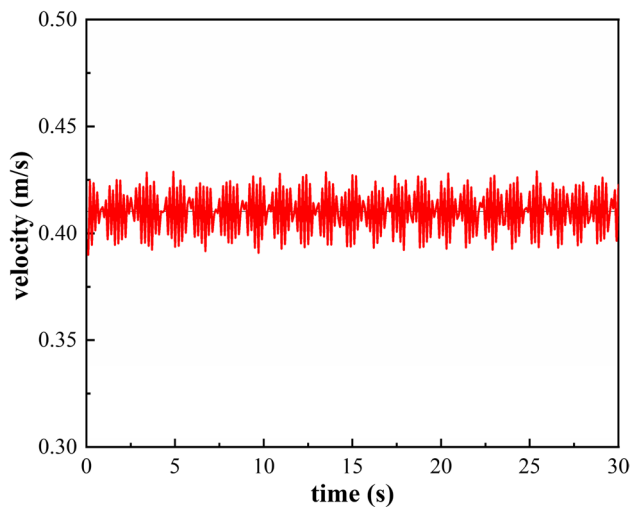
Table 1 Manual errors in measurements (Pa)		0 mL/s	66.7 mL/s	100 mL/s	166.7 mL/s	200 mL/s	266.7 mL/s
	Test 1	0.158195	3.618384	11.35016	24.22822	37.40453	58.73486
	Test 2	0.181308	3.758432	11.39164	24.24818	37.48394	58.89892
	Test 3	0.182545	3.774362	11.45445	24.26737	37.42056	58.91033
	Test 4	0.110604	3.839512	11.48745	24.34856	37.60317	58.87923
	Test 5	0.120228	3.887617	11.48007	24.35668	37.59739	58.97015
	Max	0.182545	3.887617	11.48745	24.35668	37.60317	58.97015
	Min	0.110604	3.618384	11.35016	24.22822	37.40453	58.73486
	Mean	0.150576	3.775661	11.43276	24.28980	37.50192	59.87870
	Maximum error	**0.071941**	**0.269233**	**0.13729**	**0.12846**	**0.19864**	**0.23529**

Fig. 12 Time-varying velocity at fix point. The $v_{mean} = 0.41$, $v_{max} = 0.43$, and $v_{min} = 0.39$

References

1. Arens R, McDONOUGH JM, Costarino AT et al (2001) Magnetic resonance imaging of the upper airway structure of children with obstructive sleep apnea syndrome. Am J Respir Crit Care Med 164:698–703. https://doi.org/10.1164/ajrccm.164.4.2101127

2. Shivalkar B, Van De Heyning C, Kerremans M et al (2006) Obstructive sleep apnea syndrome. J Am Coll Cardiol 47:1433–1439. https://doi.org/10.1016/j.jacc.2005.11.054

3. Arens R, McDonough JM, Corbin AM et al (2003) Upper airway size analysis by magnetic resonance imaging of children with obstructive sleep apnea syndrome. Am J Respir Crit Care Med 167:65–70. https://doi.org/10.1164/rccm.200206-613OC

4. Chen H, Li Y, Reiber JH et al (2018) Analyses of aerodynamic characteristics of the oropharynx applying CBCT: obstructive sleep apnea patients versus control subjects. Dentomaxillofacial Radiol 47:20170238. https://doi.org/10.1259/dmfr.20170238

5. Kim H-H, Rakibuzzaman M, Suh S-H et al (2018) A study of fluid dynamics parameters for prediction of obstructive sleep apnea. J Mech Sci Technol 32:1079–1085. https://doi.org/10.1007/s12206-018-0210-0

6. Kimbell JS, Basu S, Garcia GJM et al (2019) Upper airway reconstruction using long-range optical coherence tomography: effects of airway curvature on airflow resistance: NECK CURVATURE EFFECTS IN LR-OCT IMAGING. Lasers Surg Med 51:150–160. https://doi.org/10.1002/lsm.23005

7. Feng X, Chen Y, Hellén-Halme K et al (2021) The effect of rapid maxillary expansion on the upper airway's aerodynamic characteristics. BMC Oral Health 21:123. https://doi.org/10.1186/s12903-021-01488-1

8. Iwasaki T, Sato H, Suga H et al (2017) Relationships among nasal resistance, adenoids, tonsils, and tongue posture and maxillofacial form in class II and class III children. Am J Orthod Dentofacial Orthop 151:929–940. https://doi.org/10.1016/j.ajodo.2016.10.027

9. Kleinstreuer C, Zhang Z, Li Z (2008) Modeling airflow and particle transport/deposition in pulmonary airways. Respir Physiol Neurobiol 163:128–138. https://doi.org/10.1016/j.resp.2008.07.002

10. Feng X, Li G, Qu Z et al (2015) Comparative analysis of upper airway volume with lateral cephalograms and cone-beam computed tomography. Am J Orthod Dentofacial Orthop 147:197–204. https://doi.org/10.1016/j.ajodo.2014.10.025

11. Marcus CL, Brooks LJ, Ward SD et al (2012) Diagnosis and management of childhood obstructive sleep apnea syndrome. Pediatrics 130:e714–e755. https://doi.org/10.1542/peds.2012-1672

12. Mylavarapu G, Mihaescu M, Fuchs L et al (2013) Planning human upper airway surgery using computational fluid dynamics. J Biomech 46:1979–1986. https://doi.org/10.1016/j.jbiomech.2013.06.016

13. Vos W, De Backer J, Devolder A et al (2007) Correlation between severity of sleep apnea and upper airway morphology based on advanced anatomical and functional imaging. J Biomech 40:2207–2213. https://doi.org/10.1016/j.jbiomech.2006.10.024

14. Karan NB, Kahraman S (2019) Evaluation of posterior airway space after setback surgery by simulation. Med Biol Eng Comput 57:1145–1150. https://doi.org/10.1007/s11517-018-1943-8

15. Mihaescu M, Murugappan S, Kalra M et al (2008) Large Eddy Simulation and Reynolds-Averaged Navier-Stokes modeling of flow in a realistic pharyngeal airway model: An investigation of obstructive sleep apnea. J Biomech 41:2279–2288. https://doi.org/10.1016/j.jbiomech.2008.04.013

16. Luo XY, Hinton JS, Liew TT, Tan KK (2004) LES modelling of flow in a simple airway model. Med Eng Phys 26:403–413. https://doi.org/10.1016/j.medengphy.2004.02.008

17. Calmet H (2016) Large-scale CFD simulations of the transitional and turbulent regime for the large human airways during rapid inhalation. Comput Biol Med 16

18. Li C, Jiang J, Dong H, Zhao K (2017) Computational modeling and validation of human nasal airflow under various breathing conditions. J Biomech 64:59–68. https://doi.org/10.1016/j.jbiomech.2017.08.031

19. Choi J, Tawhai MH, Hoffman EA, Lin C-L (2009) On intra- and intersubject variabilities of airflow in the human lungs. Phys Fluids 21:101901. https://doi.org/10.1063/1.3247170

20. Hariprasad DS, Sul B, Liu C et al (2020) Obstructions in the lower airways lead to altered airflow patterns in the central airway. Respir Physiol Neurobiol 272:103311. https://doi.org/10.1016/j.resp.2019.103311

21. De Backer JW, Vanderveken OM, Vos WG et al (2007) Functional imaging using computational fluid dynamics to predict treatment success of mandibular advancement devices in sleep-disordered breathing. J Biomech 40:3708–3714. https://doi.org/10.1016/j.jbiomech.2007.06.022

22. Van Holsbeke C, De Backer J, Vos W et al (2011) Anatomical and functional changes in the upper airways of sleep apnea patients due to mandibular repositioning: a large scale study. J Biomech 44:442–449. https://doi.org/10.1016/j.jbiomech.2010.09.026

23. Powell NB, Mihaescu M, Mylavarapu G et al (2011) Patterns in pharyngeal airflow associated with sleep-disordered breathing. Sleep Med 12:966–974. https://doi.org/10.1016/j.sleep.2011.08.004

24. Shang Y, Dong JL, Inthavong K, Tu JY (2017) Computational fluid dynamics analysis of wall shear stresses between human and rat nasal cavities. Eur J Mech - BFluids 61:160–169. https://doi.org/10.1016/j.euromechflu.2016.09.024

25. Iwasaki T, Yanagisawa-Minami A, Suga H et al (2019) Rapid maxillary expansion effects of nasal airway in children with cleft lip and palate using computational fluid dynamics. Orthod Craniofac Res 22:201–207. https://doi.org/10.1111/ocr.12311

26. Iwasaki T, Yoon A, Guilleminault C et al (2020) How does distraction osteogenesis maxillary expansion (DOME) reduce severity of obstructive sleep apnea? Sleep Breath 24:287–296. https://doi.org/10.1007/s11325-019-01948-7

27. Jeong S-J, Kim W-S, Sung S-J (2007) Numerical investigation on the flow characteristics and aerodynamic force of the upper airway of patient with obstructive sleep apnea using computational fluid dynamics. Med Eng Phys 29:637–651. https://doi.org/10.1016/j.medengphy.2006.08.017

28. Ball CG, Uddin M, Pollard A (2008) High resolution turbulence modelling of airflow in an idealised human extra-thoracic airway. Comput Fluids 37:943–964. https://doi.org/10.1016/j.compfluid.2007.07.021

29. Hahn I, Scherer PW, Mozell MM (1993) Velocity profiles measured for airflow through a large-scale model of the human nasal cavity. J Appl Physiol 75:2273–2287. https://doi.org/10.1152/jappl.1993.75.5.2273

30. Phuong NL, Ito K (2015) Investigation of flow pattern in upper human airway including oral and nasal inhalation by PIV and CFD. Build Environ 94:504–515. https://doi.org/10.1016/j.buildenv.2015.10.002

31. Xu X, Wu J, Weng W, Fu M (2020) Investigation of inhalation and exhalation flow pattern in a realistic human upper airway model by PIV experiments and CFD simulations. Biomech Model Mechanobiol 19:1679–1695. https://doi.org/10.1007/s10237-020-01299-3

32. Mylavarapu G, Murugappan S, Mihaescu M et al (2009) Validation of computational fluid dynamics methodology used for human upper airway flow simulations. J Biomech 42:1553–1559. https://doi.org/10.1016/j.jbiomech.2009.03.035

33. Holzman RS (1998) Anatomy and embryology of the pediatric airway. Anesthesiol Clin N Am 16:707–727. https://doi.org/10.1016/S0889-8537(05)70057-2

34. Xu C, Sin S, McDonough JM et al (2006) Computational fluid dynamics modeling of the upper airway of children with obstructive sleep apnea syndrome in steady flow. J Biomech 39:2043–2054. https://doi.org/10.1016/j.jbiomech.2005.06.021

35. Cisonni J, Lucey AD, King AJC et al (2015) Numerical simulation of pharyngeal airflow applied to obstructive sleep apnea: effect of the nasal cavity in anatomically accurate airway models. Med Biol Eng Comput 53:1129–1139. https://doi.org/10.1007/s11517-015-1399-z

36. Iwasaki T, Sato H, Suga H et al (2017) Influence of pharyngeal airway respiration pressure on class II mandibular retrusion in children: a computational fluid dynamics study of inspiration and expiration. Orthod Craniofac Res 20:95–101. https://doi.org/10.1111/ocr.12145

37. Zhang Z, Kleinstreuer C (2011) Laminar-to-turbulent fluid-nanoparticle dynamics simulations: model comparisons and nanoparticle-deposition applications. Int J Numer Methods Biomed Eng 27:1930–1950. https://doi.org/10.1002/cnm.1447

38. Sherwin SJ, Blackburn HM (2005) Three-dimensional instabilities and transition of steady and pulsatile axisymmetric stenotic flows. J Fluid Mech 533https://doi.org/10.1017/S0022112005004271

39. Van Doormaal JP, Raithby GD (1984) Enhancements of the simple method for predicting incompressible fluid flows. Numer Heat Transf 7:147–163. https://doi.org/10.1080/01495728408961817

40. Cai W, Wei T, Tang X et al (2019) The polymer effect on turbulent Rayleigh-Bénard convection based on PIV experiments. Exp Therm Fluid Sci 103:214–221. https://doi.org/10.1016/j.expthermflusci.2019.01.011

41. Zhao M, Barber T, Cistulli P et al (2013) Computational fluid dynamics for the assessment of upper airway response to oral appliance treatment in obstructive sleep apnea. J Biomech 46:142–150. https://doi.org/10.1016/j.jbiomech.2012.10.033

42. Heenan AF, Matida E, Pollard A, Finlay WH (2003) Experimental measurements and computational modeling of the flow field in an idealized human oropharynx. Exp Fluids 35:70–84. https://doi.org/10.1007/s00348-003-0636-7

43. Menter FR (1994) Two-equation eddy-viscosity turbulence models for engineering applications. AIAA J 32:1598–1605. https://doi.org/10.2514/3.12149

44. Zhao M, Barber T, Cistulli PA et al (2013) Simulation of upper airway occlusion without and with mandibular advancement in obstructive sleep apnea using fluid-structure interaction. J Biomech 46:2586–2592. https://doi.org/10.1016/j.jbiomech.2013.08.010

45. Xu D, Song B, Avila M (2021) Non-modal transient growth of disturbances in pulsatile and oscillatory pipe flows. J Fluid Mech 907:R5. https://doi.org/10.1017/jfm.2020.940

46. Bates AJ, Schuh A, Amine-Eddine G et al (2019) Assessing the relationship between movement and airflow in the upper airway using computational fluid dynamics with motion determined from magnetic resonance imaging. Clin Biomech 66:88–96. https://doi.org/10.1016/j.clinbiomech.2017.10.011

47. Ma B, Lutchen KR (2006) An anatomically based hybrid computational model of the human lung and its application to low frequency oscillatory mechanics. Ann Biomed Eng 34:1691–1704. https://doi.org/10.1007/s10439-006-9184-7

48. Frank-Ito DO, Schulz K, Vess G, Witsell DL (2015) Changes in aerodynamics during vocal cord dysfunction. Comput Biol Med 57:116–122. https://doi.org/10.1016/j.compbiomed.2014.12.004
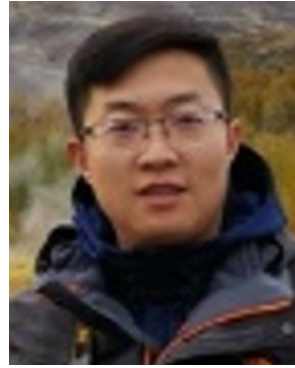
Yicheng Chen is currently proceeding his Ph.D. at Harbin Institute of Technology, China. He is conducting research in CFD and FSI with application to the human upper airway.

Xin Feng completed her Ph.D. study at the Department of clinical dentistry, University of Bergen, Norway, in 2021. Dr. Feng started to work as a postdoc at the Faculty of Medicine, University of Oslo, Norway, in August 2021.

Xieqi Shi is a clinical professor, specializing in dento-maxillofacial radiology. She is working at the Department of Clinical Dentistry, Faculty of Medicine, University of Bergen in Norge, and as a guest professor at Malmö University in Sweden. Professor Shi's research focuses on digital radiological techniques and their clinical applications.

Weihua Cai is a distinguished professor and deputy dean at the Energy and Power Engineering School of Northeast Electric Power University. He completed his Ph.D. in 2011 at HIT (Harbin Institute of Technology), China. After 2 years as a senior lecturer in HIT, he received an accelerated promotion to Associate Professor. Prof. Cai had also been at the University of Illinois at Urbana-Champaign as a visiting scholar for 12 months. He is currently conducting researches on the fundamental problem of multiphase flow and heat transfer and its application in engineered systems.

Biao Li is an associate professor at the School of Energy Science and Engineering, HIT (Harbin Institute of Technology). He is currently conducting researches in advanced flow visualization measurement technology, microfluidic in biomechanical systems, and urban canopy flow.

Yijun Zhao is a distinguished professor in the School of Energy Science and Engineering, HIT (Harbin Institute of Technology). He is currently conducting researches in the thermochemical conversion of solid fuel and comprehensive utilization of sustainable energy.